Process-dependent nanostructures of regenerated cellulose fibres revealed by small angle neutron scattering

Daisuke Sawada, Yoshiharu Nishiyama, Thomas Röder, Lionel Porcar, Hilda Zahra, Mikaela Trogen, Herbert Sixta, Michael Hummel

Polymer 218 (2021) 123510

Contents lists available at ScienceDirect

Polymer

journal homepage: http://www.elsevier.com/locate/polymer

Process-dependent nanostructures of regenerated cellulose fibres revealed by small angle neutron scattering

Daisuke Sawada [a,*], Yoshiharu Nishiyama [b], Thomas Röder [c], Lionel Porcar [d], Hilda Zahra [a], Mikaela Trogen [a], Herbert Sixta [a], Michael Hummel [a,**]

[a] Aalto University, School of Chemical Engineering, Department of Bioproducts and Biosystems, P.O. Box 16300, 00076, Aalto, Finland
[b] University Grenoble Alpes, CNRS, CERMAV, Grenoble, France
[c] Lenzing R&D, Lenzing, Austria
[d] Institut Laue Langevin, Large Scale Structures Group, 71 Avenue des Martyrs CS 20156, 38042, Grenoble, France

ARTICLE INFO

Keywords:
Regenerated cellulose fibre
Nanostructure by small angle neutron scattering
Structure-property relationship of fibre

ABSTRACT

The nanometric internal structure of polymeric fibres is fundamental for their mechanical properties. Two-dimensional small angle neutron scattering patterns were collected to obtain structural parameters of the elementary fibrils in regenerated cellulose fibres prepared by various fibre spinning technologies. Scattering features were fitted to model functions to derive parameters such as elementary fibril radius, long period of the repeating units of crystal and amorphous phase along the fibre axis, degree of orientation, and ellipticity. The correlation between structural parameters and the mechanical properties was studied for the fibres of different existing spinning processes and for the high-strength fibres. Former group showed high correlation with mechanical properties. The latter group showed generally lower correlation, but showed relatively high correlation with the long period. These structural parameters provide a basis for understanding the structure-property relationship of regenerated cellulose fibres as function of spinning types and conditions for further optimization.

1. Introduction

The nanostructures such as size and shape of crystallites, frequency of folding, localization and structure of the amorphous phase, and the interconnections of the crystalline and amorphous phase are decisive parameters for the mechanical properties of engineered fibres. The intrinsic flexibility/rigidity of a polymer chain influences the nanometric structure and mechanical properties. For example, rigid polymers like aramids can form crystals with extended chains, achieving high stiffness. However, the way of processing also influences the nanostructure. Gel-spinning can produce high stiffness fibres from flexible polyethylene and semi-rigid polyethylene terephthalate, due to the extended-chains structure in the fibre. On the contrary, melt-spinning of the same polymers results in much more extensible fibres, ascribed to chain folding and a higher share of the amorphous phase [1,2].

Cellulose is a semi-rigid polymer that exists in plant cell wall as extended single crystalline fibrils, in the crystalline form of cellulose I [3]. This is due to the synchronized process of polymerization and crystallization in the living organism. When cellulose is dissolved and coagulated or regenerated, this structural history of native cellulose is lost, and the structure formation is governed by the crystallization kinetics that depend on the physico-chemical environment. Strain, temperature, and solvent composition gradients dependent on the processing condition determine the features of the final fibre. Regenerated cellulose fibres have the crystalline form of cellulose II [4], in which the chains are packed in an anti-parallel manner, unlike the uni-directional packing of cellulose I [3]. It is also more susceptible to acid hydrolysis showing a weight loss of 2.5–7% when treated with 1 N hydrochloric acid for 24 h at 60 °C [5], clearly higher than that of hardwood pulp, ca. 2% [6], probably due to the larger fraction of amorphous cellulose.

Small angle X-ray or neutron scattering is a useful tool for studying structures at nanometer length scale. The scattering pattern of uniaxially oriented fibrous materials includes anisotropic structural information parallel (meridional) and perpendicular (equatorial) to the fibre axis, Fig. 1A. The equatorial scattering provides the cross sectional structure

* Corresponding author.
** Corresponding author.
E-mail address: daisuke.sawada@aalto.fi (D. Sawada).

https://doi.org/10.1016/j.polymer.2021.123510
Received 5 November 2020; Received in revised form 1 February 2021; Accepted 3 February 2021
Available online 11 February 2021

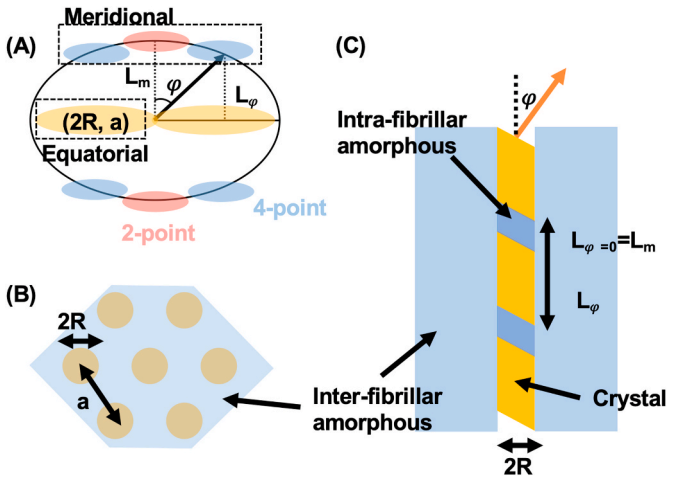

Fig. 1. (A) Typical small angle scattering pattern of fibrous polymer. (B) The cross-sectional structural model from equatorial scattering of hexagonally packed cylinders and (C) the structural model of repeating units in an elementary fibril constructed from the meridional Bragg peak.

of elementary fibrils (or lamellae crystallites) and microvoids, Fig. 1B [7,8]. On the other hand, the presence of a Bragg peak in the meridian has provided unique structural information valuable for fibre engineering [9]. The repeating structure consisting of crystalline and amorphous domains leads to the Bragg peak in the small angle scattering region. Based on the arrangement or the shape of the crystallite domains, the Bragg peak can be on the meridian or be off-meridian, Fig. 1A. The main structural models associated to the meridional Bragg peak are summarized in Fig. 1C.

Despite the indirect evidence for a periodic structure from the acid hydrolysis behaviour, the Bragg peaks of regenerated cellulose fibres are in general absent or very weak and are hidden by strong X-ray scattering due to structural features at larger length scale. Therefore, several approaches have been implemented to enhance the Bragg peak intensity through pre-treatments or by measuring neutron scattering [5,10–12]. These reports showed divergent repeating distances from the same types of cellulose fibre (supporting information Table S1), leaving open questions on the details of the periodic structure and relationship between structural parameters and mechanical properties.

In this study, small angle neutron scattering (SANS) with selective deuteration of amorphous cellulose [11] were employed to avoid alteration of the original structure in various regenerated cellulose fibres. Recently developed Ioncell fibres [13] spun from an ionic liquid, 1, 5-diazabicyclo[4.3.0]non-5-ene-1-ium acetate ([DBNH]OAc), by dry-jet wet spinning with four different spinning conditions were used for the experiment. In addition, we used regenerated cellulose fibres spun through different experimental and commercialized technologies: wet-spinning, dry-spinning and dry-jet spinning. The neutron scattering contrast between crystalline and amorphous cellulose was modulated by using D_2O vapor, D_2O in liquid form and d6-dimethyl sulfoxide (DMSO) with and without vacuum drying. The change of the scattering contrast by solvation and the fibre structure were studied by analysing the equatorial and meridional sectors, and the two-dimensional intensity distribution of the meridional Bragg peak.

2. Result and discussion

2.1. Consideration for the anisotropic scattering contrast of Ioncell fibres

One of the most significant challenges in nanostructural analysis of cellulose has been the low contrast of scattering length density (SLD) between the crystalline and amorphous phases. Acidic treatments might promote the penetration of water into amorphous phase and increase the scattering contrast between crystalline and amorphous cellulose. However, these treatments inevitably cause structural changes by collapsing the amorphous structures or interlinks between crystalline and amorphous phases. Therefore, we investigated the use of combination of neutron scattering and selective deuteration of amorphous phase by either D_2O vapor or deuterated solvents. Fig. 2A shows the scattering length density of crystalline and amorphous cellulose by a simple mixing rule with fixed molar volumes of solvents and cellulose (further details are available in supporting information). To achieve a high neutron SLD contrast (e.g. 1.0×10^{-6} Å^{-2}), perdeuteration of hydroxyl groups or the formation of a solvation shell by D_2O molecules per anhydroglucose unit is necessary.

The deuteration of the samples after the treatment with D_2O vapor was assessed by infrared spectroscopy which showed that the deuteration reached its maximum after 4 h treatment. This process significantly increased the height of the OD-stretching band, but there was still a considerable amount of OH groups left (supplementary information, Fig. S1).

Fig. 2C and D shows the SANS intensity perpendicular (equatorial) and parallel (meridional) to the fibre direction, under different swelling conditions as a function of the scattering vector Q ($Q = \frac{4\pi \sin\theta}{\lambda}$ where θ is a half of scattering angle and λ is neutron wavelength). For equatorial scattering, the intensity profiles consisted of central scattering (the scattering feature extended from unobserved low-Q region to 0.04 Å^{-1}) and a peak or a shoulder in the high Q-range between 0.04 and 0.20 Å^{-1} as illustrated in Fig. 2C. The vacuum dried sample after vapor deuteration was dominated by the central scattering whereas the others exhibited subtle or significant high-Q intensity centred approximately at 0.08 Å^{-1}. This high-Q peak indicates a density fluctuation at the length scale of the order of 10–100 Å due to the contrast between crystalline fibrils and interfibrillar amorphous region. The contrast between the two phases was low for original and vacuum dried samples, and was slightly enhanced after D_2O vapor treatment. It was significantly enhanced when the Ioncell sample was soaked in the liquid deuterosolvents. This indicates that the interfibrillar amorphous region are readily accessible to various solvent molecules when the samples are soaked in the liquid solvents.

Meridian profiles were all in the same intensity range except for the low-Q (ca. $Q < 0.025$ Å^{-1}) for the sample in D_2O (Fig. 2D). This enhanced scattering in D_2O at low-Q implies a heterogeneity at large length scale but we do not have an explanation for it at the moment. Among different conditioning options for the Ioncell fibres, only the exposure to D_2O vapor showed clear Bragg peaks in the meridian, Fig. 2B. The weight loss of the vapor treated sample after vacuum drying was about 18% by dry base, corresponding to ca. 2 residual D_2O molecules per anhydroglucose unit. However, since the bulk of the crystalline domains is anhydrous, the amorphous region contains a higher number of D_2O molecules per anhydroglucose unit. Thus, the residual D_2O molecules can be responsible for the contrast between crystalline and intrafibrillar amorphous region of meridional Bragg peak regardless of whether or not the hydroxyl groups of amorphous cellulose underwent deuterium exchange.

When the sample was soaked in DMSO-d_6 and D_2O, a shoulder in the scattering profile appeared (Fig. 2D). Assuming that the shoulder derives from a diffraction from periodic structure, the peak intensities were evaluated by curve fitting. The meridional profile was fitted with a power law function for the central scattering and a Lorentzian peak function for the Bragg peak (Table 1 and Fig. S3). Although the Bragg peak is not obvious in Fig. 2D for the sample swollen in D_2O due to the strong central scattering, the fitted diffraction intensities of the sample in liquid D_2O were slightly higher than the sample treated in vaporous D_2O. Slightly more solvation in liquid D_2O could be a reason for this observed increase, but there should not be significant difference in the number of solvated molecules for the samples in liquid and vaporous D_2O. Unlike the interfibrillar amorphous region, the intrafibrillar

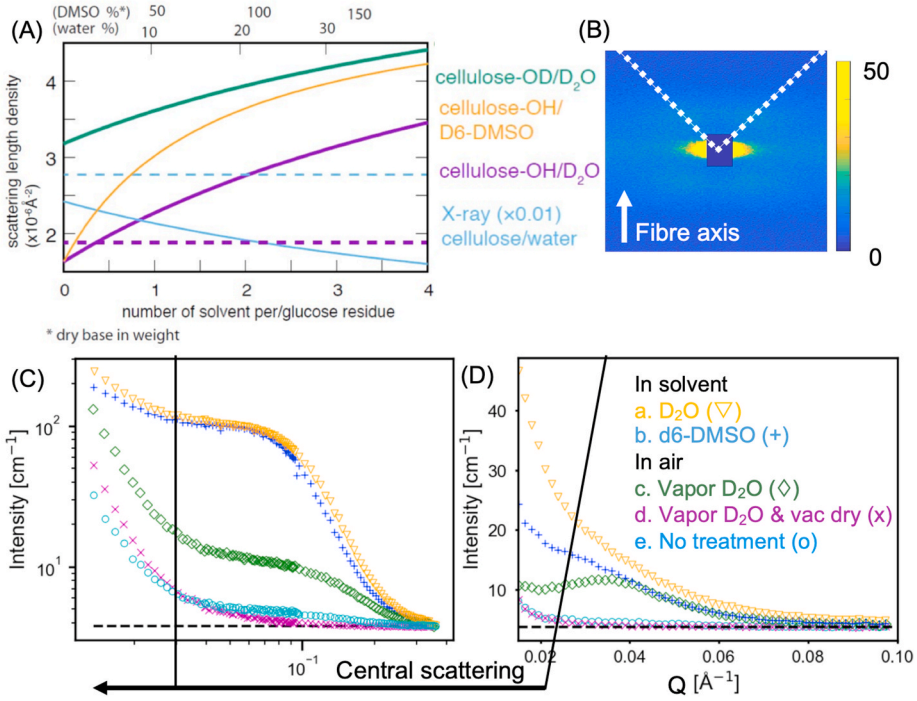

Fig. 2. (A) Neutron and X-ray scattering length density of amorphous cellulose as a function of solvation by D_2O or DMSO-d_6. Dashed line shows the scattering length density of X-ray (thin blue) and neutron (thick purple) irradiation for crystalline cellulose. (B) 2D scattering pattern and the meridional sector indicated by the white dotted line. (C) Intensity profile of the equatorial sector in logarithmic scale and (D) intensity profile of the meridian sector of an Ioncell fibre: (a) in D_2O, (b) in DMSO-d_6, (c) after vapor deuteration, (d) vapor deuteration after vacuum drying for 18 h, and (e) control sample at ambient condition. The horizontal black dashed line shows the incoherent background scattering. (For interpretation of the references to colour in this figure legend, the reader is referred to the Web version of this article.)

Table 1
Curve fitting parameters of the meridional intensity of Ioncell spun at the draw ratio of 3 after different pre-treatment protocols.

Sample	PL-exp	I (cm^{-1})	L_m (Å)	Fwhm ($Å^{-1}$)
a. In D_2O	2.3 ± 0.3	0.58 ± 0.21	242 ± 20	0.039 ± 0.004
b. In DMSO-d_6	2.5 ± 0.3	0.44 ± 0.06	217 ± 10	0.032 ± 0.002
c. Vapor D_2O	2.3 ± 0.4	0.36 ± 0.02	180 ± 5	0.031 ± 0.001
d. Vac. dry	3.3 ± 0.1	–	–	–
e. Control	3.5 ± 0.3	0.03 ± 0.00	180 ± 10	0.030 ± 0.03

I: scaling parameter of Lorentzian function, L_m: long period estimated from meridional profile, Fwhm: full width at half maximum.

amorphous region in the elementary fibril does not incorporate many solvent molecules even when the samples are soaked in the respective solvents. However, the long period of the sample in D_2O was also higher by a difference of ca. 50 Å. The higher amorphous fraction in the liquid D_2O could also increase the Bragg peak intensity when the amorphous region is the minor component of the repeating structure [14]. Thus, the elongation of amorphous fraction may also contribute to the change of Bragg peak intensity of Ioncell fibres under different solvation conditions.

Similar changes of the intensity and long period were also found in the fibres in DMSO-d_6 solvent. The meridional diffraction intensity of the sample in DMSO-d_6 was about 75% of that in D_2O and the repeating distance was shorter. This indicates that DMSO molecules can penetrate the amorphous region in the elementary fibrils but to a lesser extent compared to water.

The diffraction intensity of the D_2O vapor sample was drastically diminished after vacuum drying at 30 °C for 18 h. Although the localization of deuterated cellulose in intrafibrillar amorphous region may change the condition of neutron SLD contrast, the SLD contrast between the crystalline and amorphous phase should become close to 0 when the degree of deuteration is between 0 and 1. The high positive scattering length of the exchanged deuterium of hydroxyl groups would cancel the lower density of amorphous. Therefore, only the localized solvated molecules either by wetting or humidification can generate a structural heterogeneity to produce the strong SLD contrast between crystalline and intrafibrillar amorphous phase.

This was contrary to our first expectation that the preferential deuteration of amorphous cellulose should give enough scattering contrast for the Bragg peak to appear. Previously, Fischer et al. employed the same selective deuteration approach and mentioned vacuum drying at room temperature in their sample preparation [11] though they did not specify the term “thoroughly dry” in more detail. One possibility is that the time of vacuum drying was much shorter in their study, and tightly bound D_2O molecules might be left in the structure.

2.1.1. Structural investigations through the 1D profile analysis of the equatorial sector

Some structural parameters were obtained by fitting the equatorial scattering profiles, Fig. 3. The vacuum dried sample showed only a monotonically decreasing intensity as function of Q that can be approximated by a power law function with an exponent of 3.46. The scattering profiles from the other samples also showed a power law decay for the central scattering, but their exponents were variable by a visual inspection in limited Q-range of this study (ca. $0.013 < Q < 0.04$ $Å^{-1}$). This central scattering profile following power law function is likely due to a surface with microvoids.

Except for the vacuum dried sample, there was the scattering feature in a Q-range from 0.04 to 0.20 $Å^{-1}$. To examine the structural parameters, the equatorial intensity profiles were analysed employing the WoodSAS model [8]. The WoodSAS model can account for the cylindrical form factor of equatorial scattering with the interference function of hexagonally packed elementary fibrils.

Table 2 shows the main structural parameters from the fitting. All the other parameters are available in the supporting information Table S2. Equatorial intensity profiles from all the samples could be generally fitted with the WoodSAS model without interference function, and the addition of interference function could further improve the fitting for the samples in solvents, Fig. S2. Thus, the interference function between fibrils is enhanced in the presence of liquid solvents.

Regardless of the presence of the interference function in the fitting procedure, the diameter of elementary fibrils were estimated to be about 30 Å and 20 Å for samples in solvent and in air, respectively. The

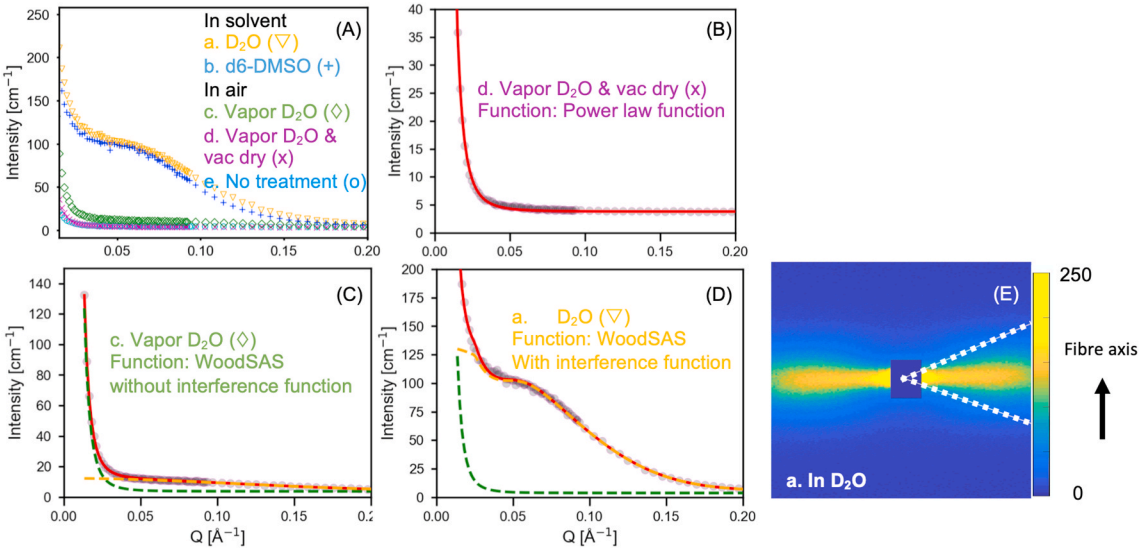

Fig. 3. (A) Equatorial intensity profile of the Ioncell spun at the draw ratio of 3 in DMSO-d_6, vacuum dried, in D_2O and D_2O vapor treated. The intensity profiles were scaled at the scattering vector Q of 0.04 $Å^{-1}$. The profiles were fitted with (B) a power-law function, (C) WoodSAS model without interference function and (D) WoodSAS model with interference function. For WoodSAS, the green and yellow dashed line represent the power law term and scattering term from the cylindrical object, respectively. (E) The 2D pattern shows the equatorial and meridional peak of the sample in liquid D_2O. The dashed white line indicates the equatorial sector. (For interpretation of the references to colour in this figure legend, the reader is referred to the Web version of this article.)

Table 2
Main structural parameters of Ioncell fibres derived from the analysis of the equatorial intensity profile of the small angle neutron scattering pattern.

WoodSAS (with interference function)	PL_exp	I_{cyl} (cm^{-1})	2R (Å)	a (Å)
a. In D_2O	3.96 ± 0.98	133.9 ± 18.0	32.2 ± 2.0	72.5 ± 4.7
b. In DMSO-d_6	3.84 ± 1.65	137.3 ± 22.1	35.0 ± 2.6	75.8 ± 4.4
WoodSAS (without interference function)	**PL_exp**	**I_{cyl} (cm^{-1})**	**2R (Å)**	
c. Vapor D_2O	3.89 ± 0.32	8.7 ± 0.8	22.0 ± 2.2	
e. Control	3.57 ± 0.44	1.2 ± 0.0	20.8 ± 0.2	
Power law function	**PL-exp**			
d. Vacuum dry	3.46 ± 0.33			

PL_exp: power law exponent, I_{cyl}: scaling parameter of intensity from cylinder, 2R: cylinder diameter, a: distance between hexagonally packed cylinders.

hydration in the crystal structure of cellulose II does not occur just by soaking in solvents [15]. The increase of 10 Å might be due to the coagulation of labile disordered chains around the elementary fibrils. Increase of one surface layer by glucose chains can expand the cellulose fibril by ca. 10 Å. This increase could be confirmed by the analysis using a Gaussian function centred at 0 $Å^{-1}$ (Guinier approximation of 2D cross section of fibre). The analyses resulted in slightly larger cylinder diameters (2R) of ca. 48 in solvent and 32 Å in air.

Distances between elementary fibrils in solvents were estimated to be 70–80 Å by the WoodSAS model, which is about double of cylindrical diameter, corresponding to a relatively low volume fraction of 0.18 through a hexagonal packing.

In addition to the WoodSAS model, we tested a Gaussian function centred at scattering feature at 0.04 $Å^{-1}$. This was to inspect the system where the correlation between fibrils dominates the scattering feature. Samples in D_2O and DMSO-d_6 could be fitted well with a broad Gaussian peak beyond a power law function (supporting information Table S2), and the packing distances were estimated to be 128 Å and 114 Å for D_2O and DMSO-d_6, respectively. However, the volume fraction of this system (ca. 0.04) was too low. For these reasons, we considered that the fitting without a cylindrical form factor was not appropriate for interpreting the structure of regenerated fibres. Fibres are dense system where the inter-fibril distances are of the similar length scale as their diameter. The form factor arising from the individual fibril cross-section and the structure factor due to the spatial arrangement of the individual fibril are difficult to be dissociated in the scattering. Thus, the fitted parameters from equatorial intensity profile should be taken as parameters with direct relation to the density fluctuation at this length scale.

2.2. *Two-dimensional intensity distribution of the meridional peak for fibres obtained via different spinning technologies*

Our first intention of studying the meridional Bragg peak was the quantification of the dimensions of the crystalline and amorphous phase in regenerated cellulose fibres. However, this was not possible due to the uncertainty in the degree of deuteration in the amorphous phase and the uncertainty of the number of solvation in the intrafibrillar amorphous region. Thus, we compared the two-dimensional intensity distribution of small angle diffraction peak patterns among different samples.

The regenerated cellulose fibres from different spinning conditions showed various intensity distributions of the correlation peak (Fig. 4). The details of these fibres are described in the Experimental section. Two wet-spun viscose fibres (Viscose and Modal) and Fortisan fibre exhibited two meridional Bragg peaks with the intensity maxima on elliptical traces. Another fibre spun via the viscose process, Super3, also exhibited two meridional diffraction spots, but its intensity maxima in the vertical trace of the Bragg peak were nearly parallel to the horizontal direction, Fig. 4D. For Bocell, the positions of the intensity maxima formed a horizontal band, Fig. 4E. However, further details were not accessible due to the exceptionally weak intensity. The fibres from dry-jet wet spinning (Ioncell and Lyocell-NMMO) showed an off-meridional pattern (Fig. 4F and G and Fig. S4), which is referred to as four-point pattern [9]. The four-point patterns showed the elliptical trace of a so-called 'eye-brow' type. The elliptical trace of four-point pattern did not match with the intensity maxima close to the co-vertex of the ellipse. It is likely that these samples contain trace amounts of a two-point pattern [16] which has a slightly different value for the long period.

Due to the elliptical shape of the meridional Bragg peak, the intensity

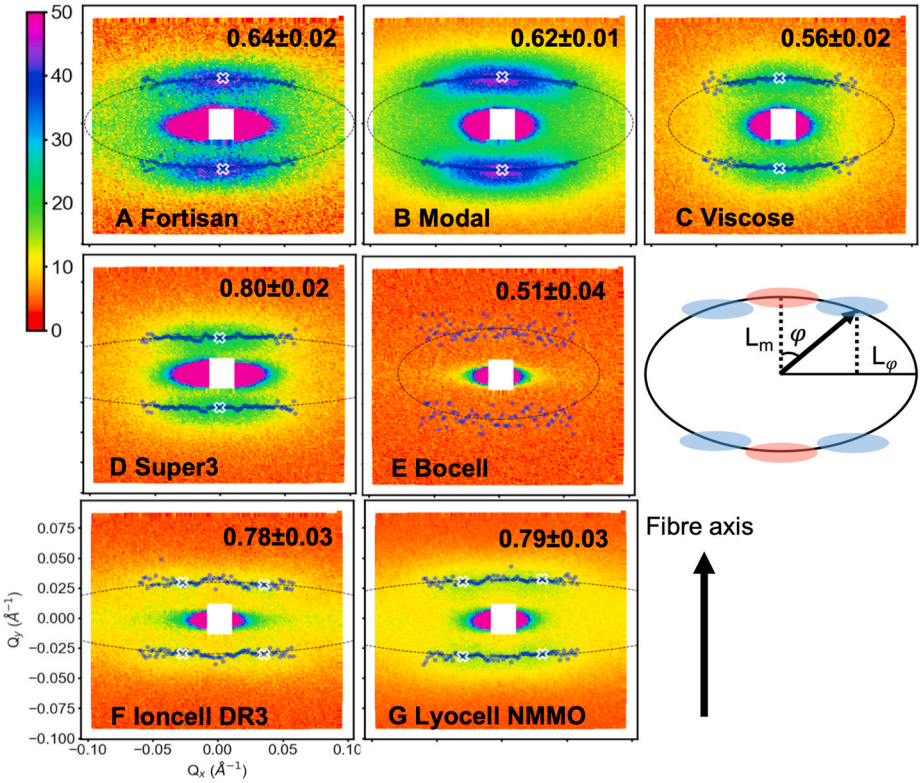

Fig. 4. Two-dimensional small angle neutron scattering pattern in absolute scale of regenerated cellulose fibres after treatment with D_2O vapor. Samples are (A) Fortisan fibre from dry spinning, (B–D) Modal, standard viscose and Super3 from wet-spinning process, (E) Bocell dry-jet spun from superphosphoric acid solution and (F, G) Ioncell and Lyocell-NMMO from dry-jet wet spinning. Intensity maxima were plotted by peak fitting of every vertical slice using three pseudo-Voigt peaks for Bragg peaks and central scattering. The dashed line represents the elliptical fit of the intensity maxima, and the number on the top of each plot shows the dimensionless ellipticity parameter. The intensity maxima of the Bragg peak are illustrated by non-filled white cross marks.

maxima of the peak along the elliptical trace were fitted with an ellipse and the dimensionless ellipticity parameter was estimated, Fig. 5 (The numerical values are available in the supporting information Table S3). We noted that the Bocell sample showed very low ellipticity. However, the Bragg peak intensity of Bocell was too low to further analyse intensity distribution.

The ellipticity parameters were in general correlated to the crystalline orientation parameters: i.e. the higher crystalline orientation, the higher ellipticity. The Fortisan sample was an outlier of this trend, and it showed very low ellipticity as compared to its crystalline orientation parameter. Also, small fluctuations of ellipticity in Ioncell samples did not match well with the fluctuations of crystalline orientation. The extensional force during the spinning process likely increases the ellipticity along with the crystalline orientation, but other factors are also contributing to the ellipticity.

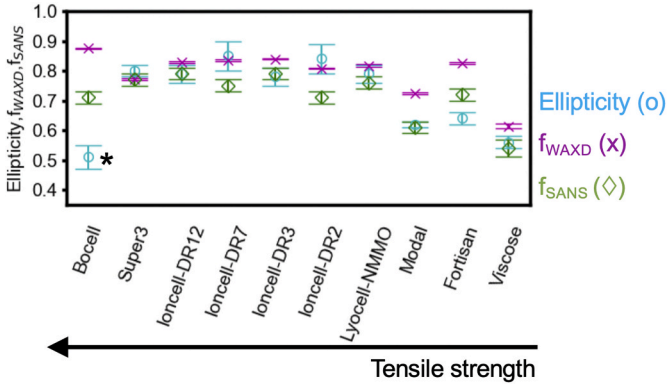

Fig. 5. Ellipticity, crystalline orientation parameter (f_{WAXD}) from X-ray diffraction, and orientation parameter of the equatorial streak by small angle neutron scattering (f_{SANS}). Samples are listed in the order of their tensile strength. High uncertainty for ellipticity of Bocell (*) due to the exceptionally low intensity of the Bragg peak.

Based on the elliptical fitting of the Bragg peak intensity, the long periods (L_m) were estimated from the fitted ellipse at the vertical position at the zero azimuthal angle ($\varphi = 0$). Lenz et al. reported similar long periods to this study for Viscose, Modal and Lyocell-NMMO after hydrolysis with 1 N hydrochloric acid at 60 °C (Table S1) [10]. The spatial arrangement of crystalline and intrafibrillar amorphous phases of the elementary fibrils might be preserved after the acid hydrolysis process. This is not surprising because macroscopic fibre length does not change after acid hydrolysis. Generally, the larger long periods were observed for high strength fibres regardless of the spinning process. However, this was not the case when comparing the fibres with similar properties such as Ioncell samples with different draw ratios from a dry-jet wet spinning process, and Modal and Viscose fibres from a wet spinning process.

For the fibres from dry-jet wet spinning with four-point patterns, the peak intensity was centred at the off-meridional spots. We define a tilt angle φ_max as the azimuthal angle to the Bragg peak position from the fibre axis. The tilt angle φ_max of about 50° in this study is on a relatively high level but an increase of φ_max of up to ca. 70° is reported for poly ethylene terephthalate fibres [17]. Murthy and Grubb [9] proposed to correlate φ_max with the internal strain of the amorphous region, which may reflect the state of coupling between crystalline and amorphous regions. They also suggested a positive correlation between φ_max and the tenacity of fibres. The obtained data in this study were not contradictory to this trend although the φ_max spanned only from 45° to 51°.

The periodicity (L_{φ_max}) along the fibre axis corresponds to the projection of the Bragg peak on the fibre axis for the four-point patterns, Table 3. Due to the high ellipticities of these samples, the L_m and L_{φ_max} were quite close.

The staggered two-dimensional alignment of crystalline and amorphous domains can generate the four-point pattern due to the tilted lattice plane of macro-lattice made of the repeating units of crystalline and amorphous domains. Without having such two-dimensional network, it is also possible to produce the four-point pattern when the crystalline domain of elementary units has an oblique shape [9]. For

Table 3
Structural parameters from elliptical fitting of the meridional Bragg peak (See Fig. 1 for the illustration of parameters). Samples are listed in the order of their tensile strength.

Sample	L_m (Å)	φ_max (°)	$L_{φ\_max}$ (Å)
Bocell	166 ± 4[a]	–	–
Super3	211 ± 2	–	–
Ioncell-DR12	210 ± 2	51 ± 3	220 ± 2
Ioncell-DR7	219 ± 3	49 ± 1	234 ± 14
Ioncell-DR3	212 ± 3	47 ± 4	214 ± 7
Ioncell-DR2	207 ± 3	47 ± 1	212 ± 8
Lyocell-NMMO	198 ± 2	45 ± 1	202 ± 8
Modal	162 ± 0	–	–
Fortisan	170 ± 1	–	–
Viscose	166 ± 1	–	–

[a] High uncertainty due to scattered intensity maxima, NMMO: *N*-methylmorpholine *N*-oxide, L_m: Long period, φ_max: angle between fibre axis and scattering vector at the intensity maxima of four-point pattern, $L_{φ\_max}$: Periodicity at the peak of four-point pattern.

regenerated cellulose fibres, the four-point pattern was observed only for the fibres from a dry-jet wet spinning process. In dry-jet wet spinning, the cellulose solution is extruded from a spinneret forming an anisotropic solution in the form of filaments in the air gap, which are then coagulated rapidly in the water bath. During this process, it is assumed that the monodisperse oriented solution is already formed in air gap mostly due to elongational stress tensors exerted through the filament draw [18]. Thus, the structure for generating four-point pattern likely occurs during the solvent diffusion into the water bath. The formation of two phases (crystal and amorphous phases) may be driven by the spinodal decomposition or nucleation of the cellulose II phase [19]. In either scenario, the structure formation in the water bath may occur sequentially from the skin to core of the single fibril with a gradient in viscosity. Due to the local asymmetry, the recrystallized cellulose II domain may have a tilted oblique shape. It is also possible that the recrystallization of cellulose II occurs from skin to core and the sequentially regenerated crystals separated by amorphous phases construct a two-dimensional staggered macro-lattice. For the fibres from wet-spinning like viscose, the solvent diffusion and orientation formation occur simultaneously in the spin bath and are affected by coagulation and chemical regeneration of the cellulose, so that the fibre cross-section becomes less homogeneous. This may induce rather random crystallite shapes (or random two-dimensional arrangement of crystalline domains), resulting in the two-point meridional pattern in the small angle scattering region. This hypothesis will be subject of our future study.

In the following discussion for structure-property relationship, Bocell sample and Fortisan sample were excluded due to their aging issues. For example, a high tensile strength of ca. 796 MPa [20] and a high modulus of 32 GPa [21] have been reported for Fortisan fibre. However, the tensile strength of Fortisan in this study was only 360 MPa and it was not possible to estimate the Young's modulus. The measured modulus and mechanical strength of Bocell was also lower than previous reports of 1.7 GPa for tensile strength and 44 GPa for modulus [21] for the same reason. In addition, the exceptionally low Bragg peak intensity of Bocell did not allow us to estimate reliable structural parameters from small angle neutron scattering. Nevertheless, we report the structural parameters of old Fortisan and Bocell samples because these high-strength regenerated cellulose fibres have often been used to study the nanostructures of regenerated cellulose fibres.

Fig. 6 shows the Pearson correlation coefficient (PCC) between nanometric structural parameters and tensile properties of regenerated cellulose fibres. The PCC is a convenient tool to show the correlation between two parameters of multiple samples, but unbiased representative sampling is important to evaluate the PCC correctly. In this study, we made two plots of PCC from fibres of different existing processes (SPIN-series, Fig. 6A) and high-strength fibres (HIGH-series, Fig. 6B).

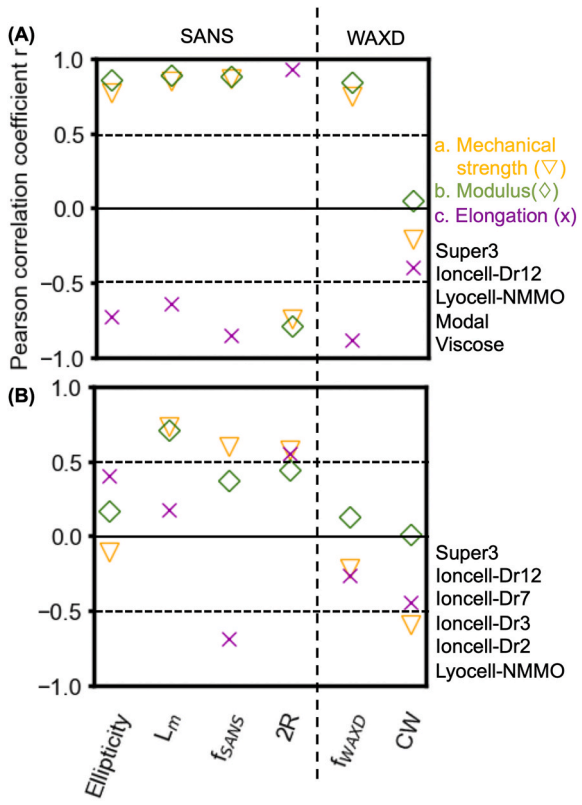

Fig. 6. Pearson correlation coefficient (r) for the structural parameters of small angle neutron scattering (SANS) and wide angle X-ray diffraction (WAXD). (A: SPIN-series) Comparison among fibres having a broad range of mechanical properties, and (B: HIGH-series) comparison among high strength fibres.

The former representatives showed generally high correlation with mechanical properties while latter did not. Although such correlation can be seen by simply plotting each parameter (Fig. S5 and Fig. S6), there may be an overestimation of PCC by the population of low-strength viscose fibres. The numerical values of these structural and mechanical properties are also available in Table 3, Table S3 and Table S4.

As has been proposed, the crystalline orientation parameter of regenerated cellulose fibres are a decisive factor for their Young's modulus and tensile strength in the SPIN-series [21]. Along with the crystalline orientation, the same structure-property trends were found for the orientation parameter from SANS and the ellipticity parameter. However, the correlation between these parameters and tensile properties are less obvious or disappeared in the HIGH-series. It is plausible that the influence of the other structural parameters on the tensile properties increases when a high level of fibre orientation is already reached, as is the case in most modern spinning technologies.

The dependence of the mechanical properties on the long period (L_m) has not been systematic. For example, Murthy et al. reported the long periods and tenacities of polyethylene terephthalate fibres prepared by different draw ratios [22]. The tenacity showed a positive correlation with the draw ratio, but the long period was correlated inversely to the tenacity except for the fibre with the highest draw ratio which has the highest tenacity and the longest long period. More recently, Litvinov et al. studied gel-spun fibres of ultrahigh molecular weight polyethylene of different draw ratios. The fibres show a negative correlation between Young's modulus and long periods [23]. Liu et al. studied four polyethylene terephthalate fibres with different mechanical properties. They reported a correlation between the long period and elongation, but did not find any correlation with the Young's modulus nor the tenacity [24]. For the cellulose polymer in our case, a general positive correlation

between the long period and both mechanical strength and Young's modulus was found for the SPIN-series, but the PCC was lower in the HIGH-series.

The crystallite width (CW) from WAXD did not show a correlation with the mechanical properties (mechanical strength, Young's modulus and fibre elongation). However, the diameter of the elementary fibril (2R), which is also a parameter of coarsening of the structure, negatively correlated with the mechanical strength and modulus. It indicates that thin elementary fibrils at the nanometer scale are not a detrimental for the strength of regenerated cellulose fibres. Such a negative correlation has also been found in polyethylene terephthalate fibres [22]. Zhu et al. proposed that the decrease of the nanometer fibril width of nanopaper is beneficial both for the ductility and mechanical strength [25], but such a relationship was not found in these series of regenerated cellulose fibres. Only the exception was the Super3 fibre whose crystal width of WAXD and mechanical properties followed this trend: i.e. it showed the small crystallite size of WAXD, its relatively high tensile strength and high elongation.

Although the long period (L_m) showed relatively high PCC in both sampling series, the other structural parameters such as tilt angle of oblique crystallites (Table 3) and amorphous distribution in the elementary fibril should be taken in account. As can be seen by the exceptionally low intensity of the Bragg peak of the Bocell sample, the amorphous fraction is probably very low since the Bragg peak intensity is a function of the amorphous fraction and the contrast of scattering length density [14]. The other fibres also showed a variation in the absolute intensity of the Bragg peak (Table S5). The volume fraction of the amorphous phase and the spatial arrangement of crystalline and amorphous phases can contribute to the mechanical strength and modulus as can be understood by the composite models of polymers [26]. Further experiments will be performed by focusing on the structure-property relationship of high-strength cellulose fibres with clarifying better contrast condition of scattering length density between crystalline and amorphous phases for X-ray or neutron scattering.

3. Conclusions

Novel cellulose solvents and advanced spinning technologies allow us to achieve high draw ratio during spinning, resulting in the high orientation of spun fibres. The spun fibres attain to a level that the influence of orientation on mechanical properties is saturated. The internal structure of elementary fibril are affected by operation conditions such as draw ratio, and can be discriminated directly from SANS pattern with selective deuteration. The control of this internal structure would be an important next step for improving the tensile properties of regenerated cellulose fibres. Thus, this work provides a basis to understand the structure-property relationship of regenerated cellulose fibres.

4. Experimental

4.1. Materials

Descriptions of regenerate cellulose fibre samples are shown in Table 4. Super3 (Cordenka), Modal (Lenzing), standard viscose fibre (Lenzing) were commercially available wet-spun viscose-type fibres. Lyocell-NMMO (Lenzing) was a commercially available dry-jet wet spun fibre. Fortisan (Celanese) was a saponified cellulose acetate prepared by the dry spinning of a solution of cellulose acetate in acetone. Bocell sample was prepared by dry-jet wet spinning of anisotropic solutions of cellulose in superphosphoric acid into acetone [21] and saponification in water/soda.

Ioncell fibres were prepared with an in-house spinning line. Spinning dope for the Ioncell fibres was prepared from birch prehydrolysis kraft pulp sheets (Enocell) and [DBNH]OAc. The cellulose pulp was grounded by a Wiley mill and added gradually into the [DBNH]OAc at 12% w/w at 80 °C. The solution was then mechanically-stirred at 30 rpm under vacuum (10–20 mbar) for 1.5 h. The solution was filtered at 20 bar pressure and spun at 68 °C, where the cellulose dope has a zero-shear viscosity of 24,000–26000 Pa s, a crossover point at an angular frequency of 0.37 s^{-1} and a modulus of 2400 Pa. The take-up and extrusion velocity were adjusted so that the spun fibres had draw ratios of 2 and 7. The collected continuous filament was finally washed in hot water (75 °C) and air-dried throughout a continuous washing line. For the draw ratios of 3 and 12 fibres, the same procedure was repeated except for a pulp concentration of 13% w/w and spinning temperature of 71 °C.

Table 4
Descriptions of regenerated cellulose fibres.

Sample	Solvent	Spinning
Bocell	Superphosphoric acid	Dry-jet
Super3	$NaOH/CS_2$	Wet
Ioncell-DR12	[DBNH]OAc	Dry-jet wet
Ioncell-DR7	[DBNH]OAc	Dry-jet wet
Ioncell-DR3	[DBNH]OAc	Dry-jet wet
Ioncell-DR2	[DBNH]OAc	Dry-jet wet
Lyocell-NMMO	NMMO	Dry-jet wet
Modal	$NaOH/CS_2$	Wet
Fortisan	Acetone	Dry
Viscose	$NaOH/CS_2$	Wet

DR: draw ratio, NMMO: *N*-methylmorpholine *N*-oxide, [DBNH]OAc: 1,5-diazabicyclo[4.3.0]non-5-enium acetate.

4.2. Fibre testing

For fibre testing, the fibre samples were conditioned at 20 ± 2 °C and relative humidity of 65 ± 2% overnight. For Ioncell fibres, the tensile properties of the fibres were measured using a Favigraph single-fibre tester (Textechno H. Stein GmbH & Co. KG, Germany) based on the standard SFS-EN 5079. The gauge length of 20 mm and test speed of 20 mm/min were used. A Vibrodyn single-fibre tester (Lenzing Instruments, Austria) was used for viscose and Fortisan fibres. Test speed was 10 mm/min and the gauge length was 20 mm. For all the fibres, standard deviations were obtained from 20 measurements.

4.3. Small angle neutron scattering (SANS)

The cellulose fibre samples were filled in a quartz tube of 3 mm diameter and vacuum dried for 3 h at 30 °C. Then, samples were deuterated by the continuous flow of moisturized argon gas bubbling through D_2O solvent (Supplementary information, Fig. S7). The degree of deuteration was determined by FT-IR by comparison of the hydrogenated and deuterated amorphous peak (Fig. S1). The degree of deuteration reached a plateau after 4 h treatment. The deuteration process was continued overnight (ca. 18 h) but no further progress of deuteration was observed after 4 h treatment. The deuterated fibres were then dried under the continuous air flow of dry argon gas for 3 h. Then, quartz tubes were quickly sealed using a wax.

Sample preparation for different swelling conditions. The Ioncell-DR3 fibres in quartz capillary were soaked in D_2O and DMSO-d_6 solvents to fully wet the samples. The DR3 Ioncell fibres in the quartz capillary prepared by vapor deuteration were vacuum dried overnight for 18 h at 30 °C. All samples were sealed in quartz capillaries with wax immediately after the preparation.

The prepared fibre samples in quartz tube were placed vertically in a sample holder. SANS data were collected at the D22 instrument at the Institut Laue Langevin, France [27]. The configuration used to reach a scattering vector Q-range of 0.01–0.45 $Å^{-1}$ were 1.5 and 5 m sample-to-detector distances, 5.6 m collimation length and a neutron wavelength of 6 Å with a 10% of wavelength band. The neutron beam size was collimated to be 1 cm × 0.1 cm (long side of rectangle parallel to fibre direction) at the sample position. Exposure times were 5–10 min.

The scattering intensity was reduced using GRASP software§ where

the data were corrected for exposure time, incident neutron flax per unit exposure area, unit solid angle for each pixels. Finally, the data were placed in the absolute scale using the direct beam measurement method.

Microscopic scattering cross section in units of cm^2 at the edge of 1.5 m detector ($\frac{d\sigma}{d\Omega_{edge}}$) which corresponds to a scattering vector Q = 0.4 $Å^{-1}$ was used to obtain the incoherent cross section of samples. Assuming the incoherent scattering of cellulose polymer was dominant, the thicknesses of the samples (T_{fibre}) were estimated from the scattering data as follows:

$$W_{fibre} = M_{cell} \frac{\frac{d\sigma}{d\Omega_{edge}} \times 10^{24}}{ICX_{glu}} \frac{1}{N_A}$$

$$T_{fibre} = \frac{W_{fibre}}{\rho_{fibre} S}$$

where W_{fibre} is a weight of the sample, M_{cell} = 162.1 is a molecular weight of a anhydroglucose monomer ($C_6H_{10}O_5$), ICX_{glu} = 868.8 (barn) is an incoherent scattering cross section per anhydroglucose unit, N_A = 6.02 × 10^{23} is the Avogadro constant, ρ_{fibre} = 1.5 (g/cm^3) is a density of the bulk cellulose fibre and S = 0.1 (cm^2) is the neutron exposure area. The calculated weights and thicknesses of the samples are shown in Table S6. Small discrepancies between measured weight and calculated weight were found, and the main reason of this was likely the failure for estimating the measured weight in a rectangle shape of neutron beam for the fibres having inhomogeneous shape. Consequently, the calculated sample thicknesses from the incoherent backgrounds were used to convert a microscopic cross section into a macroscopic cross section in units of cm^{-1}.

One dimensional (1D) SANS data analysis. 1D profile analysis were performed to elucidate the changes of structure and scattering length density (SLD) contrast between crystalline and amorphous cellulose for the directions parallel and perpendicular to fibre. 1D intensity profiles were prepared by azimuthal averaging for the horizontal direction (equator) and vertical direction (meridian) in the detector.

To determine the range for azimuthal averaging of equatorial sector, the azimuthal intensity profile for the scattering vector Q = 0.0157–0.0172 $Å^{-1}$ was fitted with a pseudo-Voigt function using a *LMFIT* software [28]. Pseudo-Voigt function is a linear combination of Gaussian and Lorentzian functions:

$$f(x) = \frac{(1-\alpha)A}{\sigma_g\sqrt{2\pi}} e^{\left[-(x-c)^2/2\sigma_g^2\right]} + \frac{\alpha A}{\pi}\left[\frac{\sigma}{(x-c)^2+\sigma^2}\right]$$

$$\sigma_g = \frac{\sigma}{\sqrt{2\ln 2}}$$

where A is the amplitude of the peak, c is the centre of the peak, σ is the half width at half maximum of the Lorentzian function., σ_g is the Gaussian equivalent of σ, and α defines the ratio of Lorentzian and Gaussian components. Thus, full width at half maximum of the function is 2σ.

The fitted azimuthal profile was used to estimate the orientation distribution of the equatorial streak $\cos^2\phi_{streak}$:

$$\cos^2\phi_{streak} = \frac{\int_0^{\pi/2} I(\phi_{streak})\sin\phi_{streak}\cos^2\phi_{streak} d\phi}{\int_0^{\pi/2} I(\phi_{streak})\sin\phi_{streak} d\phi}$$

Then it was converted into the orientation parameter (f_{SANS}) in the same fashion as the Hermans orientation parameter is estimated from the equatorial diffraction assuming cylindrical symmetry:

$$\cos^2\phi_c = 1 - 2\cos^2\phi_{streak}$$

$$f_{SANS} = \frac{3\cos^2\phi_c - 1}{2}$$

For the range of azimuthal averaging, the full width at half maximum of the pseudo-Voigt function was used. This range was selected to capture the equatorial scattering intensity in a comparable manner among samples having different azimuthal distribution and to minimize a contribution from the diffuse intensity of broad meridional diffraction peak.

Obtained equatorial intensity profiles were fitted with two models. One was a power-law function for central scattering, Gaussian function for fibril interference and constant background from incoherent scattering. Another model was the WoodSAS model developed by Penttilä et al. [8], which includes a power-law function for central scattering, a Gaussian function centred at Q = 0 $Å^{-1}$ for large pores, and scattering intensity perpendicular to fibre axis from infinitely long cylinders arranged in the hexagonal lattice:

$$I(Q) = I_{BKG} + I_{PL}Q^{-n} + Be^{\left(\frac{-Q^2}{2\sigma^2}\right)} + CI_{cyl}\left(Q, \overline{R}, \Delta R, a, \Delta a\right)$$

where I_{BKG} is the constant background from incoherent scattering, I_{PL} is the scale parameter of the power law function, n is the exponent of the power law function, B is the scale factor for Gaussian function, σ is a width parameter of Gaussian function, C is the scale parameter for the intensity from cylinder, I_{cyl} is the intensity from hexagonally packed infinitely long cylinders, $\overline{R}$ is the mean radius of a cylinder by a Gaussian distribution, ΔR is the standard deviation for R, a is the distances between cylinders and Δa is the paracrystalline distortion of a. The scale factor B was set to 0 because such scattering contribution was not observed in this study. The further details of equatorial profile fitting are described in supporting information.

The meridional Bragg peak intensity in 2D detector can only be found from a vapor deuterated sample and it should be overlapped with pronounced equatorial scattering for samples in D_2O and DMSO-d_6 solvents. To minimize the effect of equatorial scattering, the azimuthal averaging was performed in a limited range for meridional sectioning: i.e. double of the full width half maximum for equatorial scattering was excluded from the range of azimuthal averaging of meridional section. The intensity distribution of the Bragg peak was broader than the range of this averaging, and small changes in orientation distribution among samples under different sample environments were plausible. For this reason, the azimuthal averaging was performed for two different azimuthal angles of 75 and 90° to confirm the error induced by the effect of the range of averaging. Profiles were fitted with a power-law function for central scattering, a Lorentzian function for meridian Bragg peak and constant background for incoherent scattering as detailed in the supporting information. The differences of the estimated structural parameters by different integration ranges were compared. As a result, the errors induced by the different range of azimuthal averaging were smaller than the estimated error of fitting. For this reason, fitting results and estimated errors of azimuthal averaging over 90° were presented.

The ellipticity of the small angle scattering pattern was characterized from the intensity maxima around Bragg peak. The 1D longitudinal slices were exported from the GRASP software for each pixel lines of the detector. The scattering vector perpendicular to fibre axis (Q_x) of obtained 1D profile contains small fluctuation (maximum ca. 0.0004 $Å^{-1}$ at the edge of detector) based on the pixel position of the detector, but this fluctuation did not have a significant effect on the analysis on this study. The 1D profiles were fitted with three pseudo-Voigt function for the symmetrical Bragg peaks and for the central scattering. Due to the symmetrical feature of Bragg peaks, parameters of width, amplitude and ratio of the Gaussian and Lorentzian parts of two pseudo-Voigt function were restrained to be a same value. The obtained centre positions of the Bragg peak were fitted with an ellipse as follows [16]:

$$\left(\frac{1}{Q_y}\right)^2 = \left(\frac{1}{b}\right)^2 + \left(\frac{1}{a}\right)^2 \tan^2\varphi$$

where Q_y is the scattering vector parallel to fibre axis, b is the width of

semi-minor axis of ellipse, a is the width of semi-major axis, and φ is the angle between the vertical axis and the scattering vector. The dimensionless ellipticity parameter was estimated from $1-\frac{b}{a}$. Fitting was performed in the horizontal scattering vector range, $-0.06 < Q_x < 0.06$ for the two point pattern. For four-point pattern, the same range was used but the central scattering, $-0.01 < Q_x < 0.01$, were excluded from the fitting because these patterns contained a small portion of two-point pattern in this range (Fig. 4 and Fig. S4).

The long period (L_m) was estimated at the vertical intersects of the fitted ellipse:

$$L_m = \frac{2\pi}{b}$$

For four point patterns the long period (L_{φ_max}) was estimated from the scattering vector parallel to fibre axis (Q_y) at the peak intensity where the angle between fibre axis and the scattering vector (φ) is φ_max:

$$L_{\varphi\_max} = \frac{2\pi}{Q_y}$$

4.4. Wide angle X-ray diffraction (WAXD)

WAXD data were collected using a Smartlab instrument (RIGAKU) operated at 45 kV and 200 mA (λ = 1.5418 Å). The same fibre samples in capillaries used for SANS experiments were subjected to WAXD experiments. Equatorial line scans were obtained to estimate the lower bound of crystal widths (CW_{hkl}) of ($1\bar{1}0$), (110) and (020) lattice plane of cellulose II [4] by the Scherrer equation:

$$CW_{hkl} = \frac{K\lambda}{\beta_{hkl}\cos\theta}$$

where $K = 0.90$ is the shape factor, λ is the X-ray wavelength, β_{hkl} is the full width of half maximum of the diffraction peak in radians and θ is the diffraction angle of the peak. The average crystal width (CW) of three lattice planes was used due to the overlap of the peaks.

Azimuthal scans were obtained for the (020) lattice plane of cellulose II allomorph at 22.1° 2θ. The profile was used to estimate the orientation distribution between fibre axis and the crystallographic (020) lattice plane:

$$\cos^2\phi_{020} = \frac{\int_0^{\pi/2} I(\phi_{020})\sin\phi_{020}\cos^2\phi_{020}d\phi}{\int_0^{\pi/2} I(\phi_{020})\sin\phi_{020}d\phi}$$

The orientation distribution from the equatorial diffraction was then converted to the orientation distribution between fibre and crystallographic c-axis $\cos^2\phi_c$ assuming cylindrical symmetry:

$$\cos^2\phi_c = 1 - 2\cos^2\phi_{020}$$

Hermans orientation parameter (f_{WAXD}) was estimated by:

$$f_{WAXD} = \frac{3\cos^2\phi_c - 1}{2}$$

Author contributions

Daisuke Sawada: Conceptualization, Investigation, Formal analysis, Visualization, Writing - original draft. Yoshiharu Nishiyama: Conceptualization, Investigation, Formal analysis, Visualization, Writing - review & editing. Thomas Röder: Investigation, Resources, Writing - review & editing. Lionel Porcar: Investigation, Writing - review & editing. Hilda Zahra: Investigation, Resources, Writing - review & editing. Mikaela Trogen: Investigation, Resources, Writing - review & editing. Herbert Sixta: Conceptualization, Resources, Writing - review & editing. Michael Hummel: Supervision, Funding acquisition, Conceptualization, Resources, Writing - review & editing.

Notes

§https://www.ill.eu/users/support-labs-infrastructure/software-scientific-tools/grasp/

Declaration of competing interest

There are no conflicts to declare.

Acknowledgement

This work was partly funded from the Academy of Finland's Flagship Programme under Projects No. 318890 and 318891 (Competence Centre for Materials Bioeconomy, FinnCERES), and from the European Research Council (ERC) under the European Union's Horizon 2020 research and innovation programme (Grant Agreement No 715788). Fortisan sample was kindly provided by Prof. H. Chanzy, Grenoble, France. Bocell sample was kindly provided by Prof. S. Eichhorn, Manchester, UK. The tire cord sample was kindly provided by Cordenka (Obernburg, Germany). DS acknowledges the use of X-ray instrument at Aalto University at OtaNano-Nanomicroscopy Centre (Aalto-NMC). DS thanks Sauli Larkiala, Seppo Jääskeläinen and workshop team at Aalto University for their invaluable technical support. DS is grateful for suggestions and support for the deuteration experiments of cellulose fibres from Dr. Dominic Hayward at ILL science laboratory and technical support for SANS experiment from Mark Jacques at D22 beamline at ILL. DS acknowledges the use of the FTIR instrument which belongs to the Partnership for Soft Condensed Matter (PSCM). The authors thank ILL for the allocation of beamtime at the D22 instrument.

Appendix A. Supplementary data

Supplementary data to this article can be found online at https://doi.org/10.1016/j.polymer.2021.123510.

References

[1] P.J. Lemstra, R. Kirschbaum, Speciality products based on commodity polymers, Polymer 26 (9) (1985) 1372–1384, https://doi.org/10.1016/0032-3861(85)90315-5.
[2] P. Lemstra, N. Van Aerle, C. Bastiaansen, Chain-extended polyethylene, Polym. J. 19 (1) (1987) 85–98, https://doi.org/10.1295/polymj.19.85.
[3] Y. Nishiyama, P. Langan, H. Chanzy, Crystal structure and hydrogen-bonding system in cellulose Iβ from synchrotron X-ray and neutron fiber diffraction, J. Am. Chem. Soc. 124 (31) (2002) 9074–9082, https://doi.org/10.1021/ja0257319.
[4] P. Langan, Y. Nishiyama, H. Chanzy, X-ray structure of mercerized cellulose II at 1 Å resolution, Biomacromolecules 2 (2) (2001) 410–416, https://doi.org/10.1021/bm005612q.
[5] J. Lenz, J. Schurz, E. Wrentschur, The length of the crystalline domains in fibres of regenerated cellulose. Determination of the crystallite length of cellulose II by means of wide-angle X-ray diffraction and transmission electron microscopy, Holzforschung 42 (2) (1988) 117–122, https://doi.org/10.1515/hfsg.1988.42.2.117.
[6] H. Håkansson, P. Ahlgren, Acid hydrolysis of some industrial pulps: effect of hydrolysis conditions and raw material, Cellulose 12 (2) (2005) 177–183, https://doi.org/10.1007/s10570-004-1038-6.
[7] H. Jakob, S. Tschegg, P. Fratzl, Hydration dependence of the wood-cell wall structure in Picea abies. A small-angle X-ray scattering study, Macromolecules 29 (26) (1996) 8435–8440, https://doi.org/10.1021/ma9605661.
[8] P.A. Penttilä, L. Rautkari, M. Österberg, R. Schweins, Small-angle scattering model for efficient characterization of wood nanostructure and moisture behaviour, J. Appl. Crystallogr. 52 (2) (2019) 369–377, https://doi.org/10.1107/S1600576719002012.
[9] N. Murthy, D. Grubb, Tilted lamellae in an affinely deformed 3D macrolattice and elliptical features in small-angle scattering, J. Polym. Sci. B Polym. Phys. 44 (8) (2006) 1277–1286, https://doi.org/10.1002/polb.20778.
[10] K. Stana-Kleinschek, V. Ribitsch, T. Kreže, M. Sfiligoj-Smole, Z. Peršin, Correlation of regenerated cellulose fibres morphology and surface free energy components, Lenzinger Berichte 82 (1) (2003) 83–95.
[11] E. Fischer, P. Herchenröder, R.S.J. Manley, M. Stamm, Small-angle neutron scattering of selectively deuterated cellulose, Macromolecules 11 (1) (1978) 213–217, https://doi.org/10.1021/ma60061a039.
[12] H. Kiessig, in: Das Papier, vol. 22, 1968, pp. 261–269.

[13] H. Sixta, A. Michud, L. Hauru, S. Asaadi, Y. Ma, A.W. King, I. Kilpeläinen, M. Hummel, Ioncell-F: a high-strength regenerated cellulose fibre, Nord. Pulp Pap Res. J. 30 (2015) 43–57, https://doi.org/10.3183/npprj-2015-30-01-p043-057.
[14] Y. Nishiyama, U. Kim, D. Kim, K.S. Katsumata, R.P. May, P. Langan, Periodic disorder along ramie cellulose microfibrils, Biomacromolecules 4 (4) (2003) 1013–1017, https://doi.org/10.1021/bm025772x.
[15] K. Kobayashi, S. Kimura, E. Togawa, M. Wada, Crystal transition from Na–cellulose IV to cellulose II monitored using synchrotron X-ray diffraction, Carbohydr. Polym. 83 (2) (2011) 483–488, https://doi.org/10.1016/j.carbpol.2010.08.006.
[16] N. Murthy, D. Grubb, K. Zero, Structural implications of the elliptical form of small-angle reflections in oriented semicrystalline polymers, Macromolecules 33 (3) (2000) 1012–1021, https://doi.org/10.1021/ma9911501.
[17] E. Perret, F.A. Reifler, R. Hufenus, O. Bunk, M. Heuberger, Modified crystallization in PET/PPS bicomponent fibers revealed by small-angle and wide-angle X-ray scattering, Macromolecules 46 (2) (2012) 440–448, https://doi.org/10.1021/ma3021213.
[18] H.A. Cousley, S.B. Smith, The formation and structure of a new cellulosic fibre, Lenzinger Berichte 75 (1995) 51–61.
[19] Y. Nishiyama, S. Asaadi, P. Ahvenainen, H. Sixta, Water-induced crystallization and nano-scale spinodal decomposition of cellulose in NMMO and ionic liquid dope, Cellulose 26 (1) (2019) 281–289, https://doi.org/10.1007/s10570-018-2148-x.
[20] J.C. Smith, F.L. McCrackin, H.F. Schiefer, W.K. Stone, K.M. Towne, Stress-strain relationships in yarns subjected to rapid impact loading: 4. Transverse impact tests, J. Res. Natl. Bur. Stand. 57 (1956) 83–89, https://doi.org/10.1177/004051755602601101.
[21] M. Northolt, H. Boerstoel, H. Maatman, R. Huisman, J. Veurink, H. Elzerman, The structure and properties of cellulose fibres spun from an anisotropic phosphoric acid solution, Polymer 42 (19) (2001) 8249–8264, https://doi.org/10.1016/S0032-3861(01)00211-7.
[22] N. Murthy, D. Grubb, K. Zero, C. Nelson, G. Chen, Lamellar structure and properties in poly (ethylene terephthalate) fibers, J. Appl. Polym. Sci. 70 (12) (1998) 2527–2538, https://doi.org/10.1002/(SICI)1097-4628(19981219)70:12<2527::AID-APP27>3.0.CO;2-J.
[23] V. Litvinov, J. Xu, C. Melian, D. Demco, M. Moller, J. Simmelink, Morphology, chain dynamics, and domain sizes in highly drawn gel-spun ultrahigh molecular weight polyethylene fibers at the final stages of drawing by SAXS, WAXS, and 1H solid-state NMR, Macromolecules 44 (23) (2011) 9254–9266, https://doi.org/10.1021/ma201888f.
[24] Y. Liu, L. Yin, H. Zhao, G. Song, F. Tang, L. Wang, H. Shao, Y. Zhang, Insights into process–structure–property relationships of poly (ethylene terephthalate) industrial yarns by synchrotron radiation WAXD and SAXS, J. Appl. Polym. Sci. 132 (36) (2015), https://doi.org/10.1002/app.42512.
[25] H. Zhu, S. Zhu, Z. Jia, S. Parvinian, Y. Li, O. Vaaland, L. Hu, T. Li, Anomalous scaling law of strength and toughness of cellulose nanopaper, Proceedings of the National Academy of Sciences of the USA 112 (29) (2015) 8971–8976, https://doi.org/10.1073/pnas.1502870112.
[26] D. Grubb, A structural model for high-modulus polyethylene derived from entanglement concepts, J. Polym. Sci. Polym. Phys. Ed 21 (2) (1983) 165–188, https://doi.org/10.1002/pol.1983.180210201.
[27] D. Sawada, Y. Nishiyama, L. Porcar, T. Roeder, Study of Periodic Disorder in Regenerated Cellulose Fibers by Small Angle Neutron Diffraction, Institut Laue-Langevin (ILL), 2019, https://doi.org/10.5291/ILL-DATA.9-11-1936.
[28] M. Newville, T. Stensitzki, D.B. Allen, M. Rawlik, A. Ingargiola, A. Nelson, LMFIT: Non linear least-square minimization and curve-fitting for Python, Astrophysics Source Code Library (2016) ascl: 1606.014.